Journal of Materials Chemistry A

ROYAL SOCIETY OF CHEMISTRY

PAPER

View Article Online
View Journal

Cite this: DOI: 10.1039/d6ta00905k

Cu(II)/Fe(II) electron-deficient pairs as bifunctional catalysts for efficient PMS activation and solar-driven water evaporation

Wanyu Zhang,†[a] Xixing Wang,†[a] Danhong Shang,[a] Linzhi Zhai,[a] Xiaobo Zhang,*[c] Fu Yang *[a] and Edison Huixiang Ang *[b]

Addressing the dual challenges of organic wastewater purification and freshwater regeneration requires innovative materials capable of multifunctional integration. This study presents a tactical design of metallic Cu-interfaced FeO composites (Fe/Cu-*x*) synthesized *via* a synergistic self-assembly and pyrolysis strategy. The interfacial Cu/FeO pairs, featuring electron-deficient Cu(II) and Fe(II) pairs along with promoted oxygen vacancies, afford abundant redox cycles to enable exceptional electron transfer and peroxymonosulfate (PMS) activation. The optimized Fe/Cu-800 catalyst achieved an excellent tetracycline (TC) degradation efficiency (k_{obs} = 0.235 min^{-1}) within 20 min, far outperforming the other controls including the Cu-free one and different temperature-derived, retained robust performance across wide pH ranges and in real water matrices, and exhibited rational recyclability. The dominant ·OH alongside other free radicals synergistically contribute to the TC degradation. Beyond catalysis, this study demonstrates the customizable integration of the powder catalyst into a monolithic form evaporator through a Ca^{2+}-triggered hydrogel crosslinking strategy. This uniquely integrated system simultaneously accomplishes pollutant degradation and solar-driven clean water production. Under 1 sun irradiation, the evaporator achieved a TC degradation rate of 94.4% within 20 minutes and simultaneously realized a high-water evaporation rate of 1.313 kg m^{-2} h^{-1}, demonstrating a significant dual-functional synergy effect. This research breaks the conventional single-function limitation by offering a novel "degrade-and-evaporate" platform, which emerges from precise interfacial engineering and modular device integration. It provides a sustainable and efficient technical pathway for integrated wastewater treatment and water resource regeneration.

Received 30th January 2026
Accepted 7th May 2026

DOI: 10.1039/d6ta00905k

rsc.li/materials-a

1. Introduction

The ubiquitous occurrence of antibiotics in aquatic environments and their associated ecotoxicological effects have emerged as a focal issue in global environmental research.[1] Tetracycline (TC), a representative broad-spectrum antimicrobial agent, has been extensively deployed in clinical medicine, livestock farming, and aquaculture owing to its superior bacteriostatic activity, cost-effectiveness, and efficacy against both Gram-positive and Gram-negative bacteria.[2] However, the limited removal efficiency of conventional wastewater treatment processes has led to the continuous discharge of TC into surface water, groundwater, and soil matrices *via* point and non-point sources.[3,4] The inherent chemical recalcitrance of TC compounds confers pronounced environmental persistence, and the long-term accumulation of parent molecules and metabolites not only poses ecotoxicity risks but also drives the horizontal transfer and dissemination of antibiotic resistance genes (ARGs) among environmental microbial communities, thereby posing far-reaching threats to ecosystem stability and public health security.[5,6] Accordingly, the development of novel remediation technologies capable of achieving both efficient pollutant mineralization and water resource regeneration has become a critical scientific challenge in this field.

Advanced Oxidation Processes (AOPs) are effective for degrading persistent organic pollutants like TC in wastewater, primarily by generating reactive oxygen species (ROS) to mineralize contaminants.[7] Peroxymonosulfate (PMS) has been widely studied in AOPs due to its easily activated asymmetric structure.[8] Despite PMS possessing high oxidation potential, its O–O bond dissociation kinetics are limited in the absence of catalysts, hindering the spontaneous generation of reactive oxygen species necessary for effective pollutant degradation.[9]

[a]School of Environmental and Chemical Engineering, Jiangsu University of Science and Technology, Zhenjiang 212100, Jiangsu, China. E-mail: fuyang@just.edu.cn
[b]Natural Sciences and Science Education, National Institute of Education, Nanyang Technological University, Singapore, 637616, Singapore. E-mail: edison.ang@nie.edu.sg
[c]Department of Radiology, First Medical Center, Chinese People's Liberation Army General Hospital, Beijing, China. E-mail: zhangxiaobo301@126.com
† Equal contribution.

Consequently, developing efficient catalytic systems to activate PMS has become crucial. Transition metals (*e.g.*, Fe(II)) for PMS activation afford great promise in AOPs, but Fe(II) is rapidly oxidized to Fe(III) and regenerates slowly, limiting reaction efficiency.[10] Introducing a second metal creates a bimetallic synergetic site that enhances PMS adsorption and electron transfer, which facilitates interfacial electron coupling and accelerates Fe(II) regeneration through synergistic redox cycling.[11] By forming tightly coupled electronic interfaces with transition metal oxides, copper-based metals often modulate the electronic structure of active centers, thereby enhancing PMS activation.[12] For example, Shao *et al.* showed that CuO, as the main active site on Fe_3O_4 in Fe_3O_4@CuO_x composites, promotes efficient tetracycline mineralization *via* $^1O_2$.[13] Similarly, Akram *et al.* reported that Fe–Cu coupling in Fe_3O_4/CuO nanocomposites facilitates interfacial electron transfer, enabling efficient photocatalytic dye degradation.[14] These studies highlight the dual function of Cu-based materials in providing physical dispersion and modulating the electronic structure, thereby enhancing the Fe^{2+}/Fe^{3+} redox cycle. The catalytic performance of bimetallic catalysts is largely influenced by the refined electronic state and their electronic coupling through metal–support interactions. While constructing defined support–metal frameworks can modulate catalytic activity of interfacial active species, achieving effective synergy remains challenging.[15]

Inspired by the above thoughts, we leveraged a dopamine triggered modification strategy to construct Cu interfaced FeO hybrid composites (Cu/FeO) through *in situ* polymerization and carbonization processes. By regulating the synthesis temperature, nanoscale metallic copper is effectively anchored onto FeO, forming abundant Cu(II)/Fe(II) electron-defect pairs and enabling enhanced redox cycling *via* interfacial electron transfer.[16,17] In contrast to Fe_3O_4-800—which eliminates interference from carbon support effects and temperature-induced phase transitions—the improved performance of the Cu/FeO composite interface is attributed to the incorporation of Cu. This facilitates the regeneration of Fe(II), promotes sustained activation of PMS, and enhances the generation of reactive oxygen species (ROS). To further expand the functionality of the catalysts in the synchronous decontamination and freshwater regeneration, the catalyst was incorporated into a two-dimensional glass fiber substrate to construct a monolithic photothermal evaporator, which can be applied to photothermal evaporation coupled with pollutant degradation.[18] This work affords an efficient approach to address wastewater treatment and clean water regeneration.

2. Experimental section

2.1. Materials and reagents

Sodium acetate (CH_3COONa, AR), ethylene glycol ($C_2H_6O_2$), dopamine hydrochloride ($C_8H_{12}ClNO_2$), methanol (99.9%, CH_3OH), *tert*-butanol (99.5%, $C_4H_{10}O$), L-histidine (99%, $C_6H_9N_3O_2$), *p*-benzoquinone (98%, $C_6H_4O_2$), potassium peroxymonosulfate triple salt (PMS), and sodium hydroxide (NaOH, AR) were purchased from Energy Co, Ltd. Copper(II) acetate monohydrate ($Cu(CH_3COO)_2 \cdot H_2O$, AR) and tetracycline (TC, CP, $C_{22}H_{24}N_2O_8$) were obtained from Shanghai Macklin Biochemical Co., Ltd. Sodium chloride (99.7%, NaCl), sodium carbonate (Na_2CO_3, AR), sodium bicarbonate (99.5%, $NaHCO_3$), sodium sulfate (99.5%, Na_2SO_4), and sodium dihydrogen phosphate (NaH_2PO_4, AR) were purchased from Shanghai Aladdin Industrial Co., Ltd. Ferric chloride hexahydrate ($FeCl_3 \cdot 6H_2O$, AR) was obtained from Xiya Reagent.

2.2. Preparation of Fe_3O_4

Fe_3O_4 particles were synthesized *via* a solvothermal method.[19] Briefly, 3.40 g of $FeCl_3 \cdot 6H_2O$ and 6.0 g of CH_3COONa were dissolved in 100 mL of ethylene glycol. The mixture was ultrasonicated for 90 min and then transferred into a 200 mL Teflon-lined stainless-steel autoclave. The autoclave was sealed and maintained at 190 °C for 10 h. After cooling naturally to room temperature, the product was collected by centrifugation, washed three times with ethanol, and dried under vacuum at 65 °C.

2.3. Synthesis of Fe/Cu-*x*

Fe_3O_4 (1 g) was ultrasonically dispersed in 100 mL methanol (solution A). Separately, dopamine hydrochloride (100 mg) and Cu(II) acetate monohydrate (1 mmol) were dissolved in 50 mL methanol under stirring (solution B). Solution B was added dropwise to solution A and stirred at 400 rpm for 12 h. The product was collected by centrifugation, washed, and vacuum-dried at 70 °C for 12 h.[20] Finally, the solid was calcined under N_2 at 5 °C min^{-1} to 800 °C and held for 3 h, yielding Fe/Cu-800. Comparative samples Fe/Cu-700 and Fe/Cu-900 were prepared similarly at respective temperatures.

2.4. Characterization

The surface morphology and elemental composition of the prepared materials were examined by scanning electron microscopy (SEM, S4800, Hitachi, Japan). Transmission electron microscopy (TEM) and energy-dispersive X-ray spectroscopy (EDX) analyses were conducted on a JEM-2010 EX microscope (JEOL, Japan). X-ray photoelectron spectroscopy (XPS) measurements were performed on a PHI 5000 Versa Probe spectrometer (ULVAC-PHI, Japan) with Al Kα radiation, and the binding energies were calibrated using the C 1s peak at 284.6 eV. The crystalline phases of the samples were characterized by X-ray diffraction (XRD, XRD-6000X, Shimadzu, Japan) with Cu Kα radiation. Electrochemical measurements, including open circuit voltage (OCV), cyclic voltammetry (CV), and electrochemical impedance spectroscopy (EIS), were carried out on a CHI760E workstation using a standard three-electrode system with a Pt counter electrode and an Ag/AgCl reference electrode. Photothermal performance was evaluated under simulated sunlight generated using a Solar 500 T solar simulator (Beijing Newbit Technology). Infrared thermal images were captured using a UTi260B thermal imager (UNIT, China) with the samples placed on a hydrated polymer membrane.

2.5. Catalytic performance evaluation

The catalytic performance of the materials was evaluated through tetracycline (TC) degradation experiments using peroxymonosulfate (PMS) as the oxidant. The tests were conducted in a 100 mL beaker containing 50 mL of TC solution (0.02 g L^{-1}) under continuous stirring. After adding 10 mg of PMS and 10 mg of the catalyst, the reaction kinetics were monitored using a UV spectrophotometer (MAPADA P1800). During the reaction, 2–3 mL aliquots were collected at specified intervals for analysis, with the initial solution used as a blank control (Text S1).

To assess reusability, the catalyst was recovered after each cycle *via* magnetic separation, washed successively with ethanol and deionized water, and dried at 60 °C. The regenerated catalyst was then reintroduced into a fresh TC solution containing PMS to initiate the next degradation cycle.

2.6. Evaluation of photothermal evaporation performance

The multifunctional catalyst was embedded into a monolithic, recyclable evaporator based on glass fiber to simultaneously degrade pollutants and regenerate clean water *via* photothermal evaporation. Specifically, 20 mg of the catalyst was uniformly dispersed in 6 mL of deionized water containing 14 mg of sodium alginate under vigorous stirring. The resulting suspension was drop-cast onto bulk glass fibers, which were then immersed in a calcium chloride solution for cross-linking and solidification to obtain free-standing photothermal evaporators.

The evaporation test was conducted by placing an evaporator loaded with the catalyst on the surface of 50 mL tetracycline solution (20 mg L^{-1}) inside a beaker. The setup was irradiated under a solar simulator with light intensity calibrated to 1 kW m^{-2} (1 sun) using an optical power meter (FZ400, Beidian, China). Surface temperature was recorded every 10 minutes using an infrared thermal imager, while the mass loss of water was monitored in real time over 60 minutes with an electronic balance. The photothermal conversion efficiency and water evaporation rate were subsequently calculated from the collected data.

3. Results and discussion

3.1. Morphological and structural analysis

Fig. 1a outlines the synthesis of the Fe–Cu bimetallic catalysts. Initially, polydopamine was assembled on the prepared Fe_3O_4 nanospheres, followed by the *in situ* anchoring of Cu(II) species. Subsequently, Fe/Cu-800 composites were obtained by calcination under N_2. This design features a synergistic interplay between Cu species as secondary active sites for enhanced electron transfer and FeO as the primary active center, which provides structural support and facilitates redox cycling. The strong interaction between the two metals results in a bifunctional material with high activity and stability, demonstrating promising potential for water purification applications. Scanning electron microscopy (SEM) images of Fe/Cu-800 (Fig. 1b and S1) revealed an irregular spherical configuration with visible copper nanoparticles. Transmission electron microscopy (TEM, Fig. 1c) indicates that the Fe/Cu-800 featured nanospherical configuration with the distribution of some Cu particles, which was confirmed by high-resolution transmission electron microscopy (HRTEM, Fig. 1d–f), indicative of distinct lattice fringes of 0.45 nm and 0.20 nm corresponding to the Fe (400) and Cu (111) crystal planes (Fig. S2). This confirms the coexistence of iron and copper phases and verifies that the Cu species (~8.6 nm) form closely integrated interfaces with the FeO substrate. High-angle annular dark-field scanning transmission electron microscopy (HAADF-STEM) combined with energy-dispersive X-ray spectroscopy (EDX) elemental mapping (Fig. 1g) demonstrated the high dispersity of Cu onto FeO attached by bits of nitrogen modified carbon, which provides more accessible surface active sites for subsequent catalytic reactions. Notably, the surface nitrogen species possibly acted as polar sites to trigger the enrichment of pollutants and accelerate the reaction kinetics.

3.2. Surface properties and crystalline state analysis

The crystal structures of Fe/Cu-700, Fe/Cu-800, and Fe/Cu-900 were examined by X-ray diffraction (XRD). As shown in Fig. 2a, distinct diffraction peaks corresponding to FeO appeared at 41.9° and 60.8° in Fe/Cu-800 and Fe/Cu-900, but not in Fe/Cu-700, indicating the partial reduction of Fe_3O_4 to the FeO phase at higher temperatures. The distinct diffraction peaks of copper confirm the successful loading of metallic Cu onto the carbon-coated FeO surface.[21] Figure S3 presents the Raman spectra of the Fe/Cu series. For Fe/Cu-800, the characteristic D band (defective carbon) and G band (graphitized carbon) appear at 1350 cm^{-1} and 1580 cm^{-1}, respectively.[22] The I_D/I_G ratio of 0.91 indicates the formation of a partially graphitized carbon matrix with a moderate defect density, which facilitates interfacial electron transfer. In contrast, Fe/Cu-700 exhibits relatively weak carbon-related signals, while a broadened scattering peak characteristic of Fe_3O_4 appears in the low-frequency region, suggesting that the iron phase predominantly exists as Fe_3O_4 at this pyrolysis temperature.[23] For Fe/Cu-900, the intensities of both the D and G bands decrease significantly, likely due to thermal decomposition of the carbon layer at excessively high temperatures, leading to damage of the graphitized carbon framework. These results demonstrate that controlled regulation of the pyrolysis temperature not only drives the transformation of the Fe phase but also governs the evolution of the defective carbon structure, thereby enhancing interfacial electron transfer and optimizing the overall catalytic performance of the material.[24] The surface elemental composition of the catalyst, confirmed by X-ray photoelectron spectroscopy (XPS) analysis (Fig. 2b–f and S4), further verified the presence of C, N, O, Fe, and Cu elements. The C 1s XPS spectra revealed three deconvoluted peaks at 284.8 eV, 285.8 eV, and 289 eV for the Fe/Cu-800 catalyst, attributed to C–C, C–N and C=O bonds, respectively (Fig. 2b), indicative of surface carbon and functional species of the catalyst. The high-resolution N 1s XPS spectra revealed characteristic peaks at 398.8 eV and 400.4 eV, attributable to pyridinic nitrogen and pyrrolic

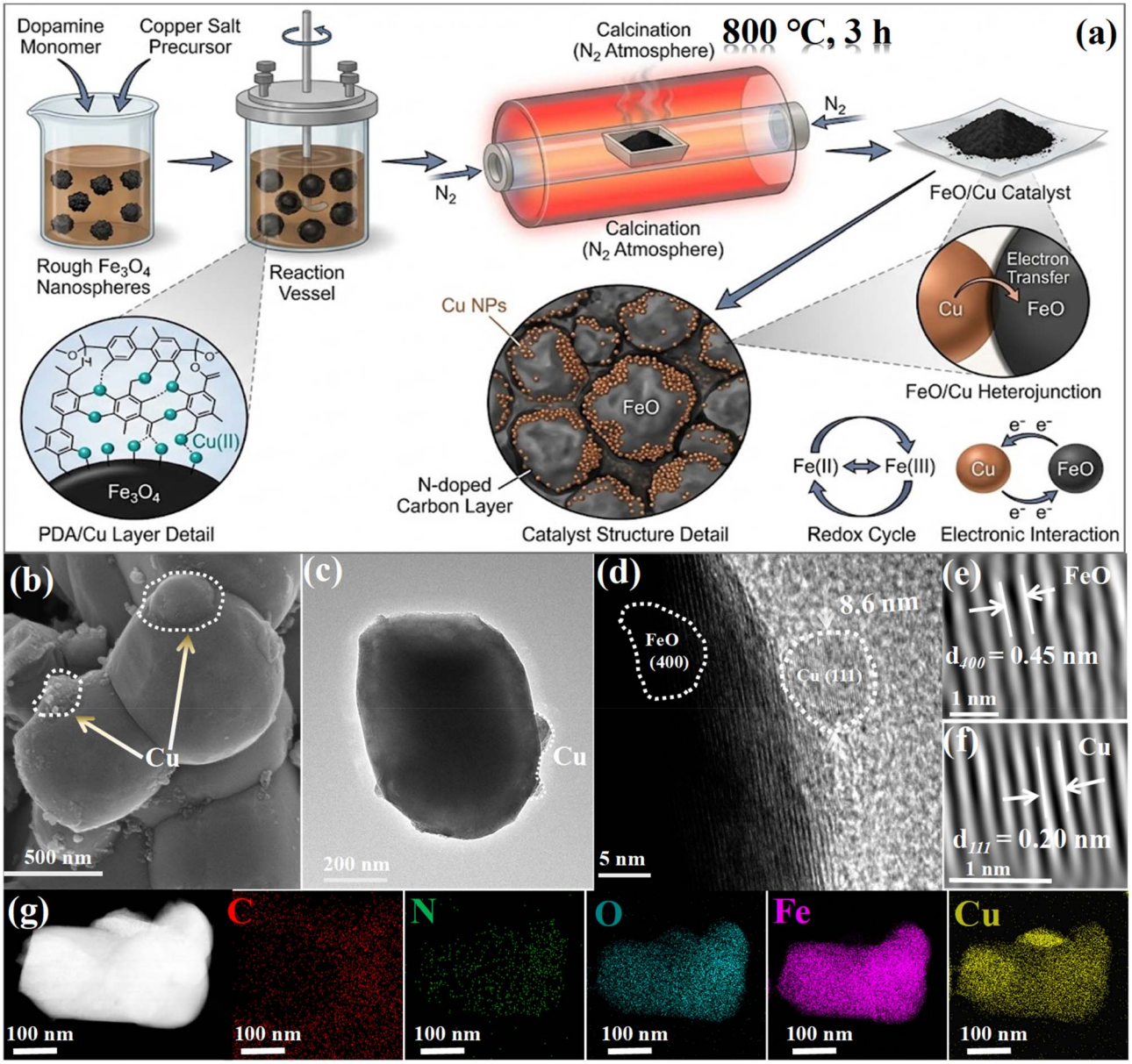

Fig. 1 (a) Schematic synthesis of the Fe/Cu-800 catalyst. (b) Representative SEM image, (c) TEM image, and (d) HRTEM image of Fe/Cu-800; (e and f) FeO (400), and Cu (111) planes in Fe/Cu-800 extracted from fast Fourier transform and (g) HAADF-STEM images and corresponding elemental mapping images of Fe/Cu-800.

nitrogen, respectively (Fig. 2c). The existing pyridinic nitrogen with strong Lewis basicity readily coordinated with transition metals to serve as a metal-anchoring site that improves the surface microenvironment.[25] Meanwhile, pyrrolic nitrogen facilitates the carrier's electron supply capacity and interfacial charge transfer, establishing a smoother electron transport pathway.[26] The O 1s spectra verified the existence of lattice oxygen (O_L, 529.5 eV), deficient oxygen (O_v, 530.8 eV), and surface-adsorbed oxygen (O_s, 531.6 eV).[27,28] Compared to Fe/Cu-700, Fe/Cu-800 exhibits a reduced relative proportion of O_L, aligning with the trend of partial reduction of Fe_3O_4 to FeO. In addition, Fe/Cu-800 exhibited a higher oxygen vacancy (O_v) concentration, which facilitates the adsorption of oxidant species.[29] Fig. 2e shows that the Cu 2p XPS spectra of all three catalysts exhibit characteristic peaks corresponding to Cu^0, Cu^{2+}, and satellite states. Notably, Fe/Cu-800 exhibits a more pronounced positive shift compared to Fe/Cu-700 and Fe/Cu-900, creating electron-deficient Cu(II), attributed to stronger metal interactions and interfacial charge transfer, which enables loss of electrons from Cu^{2+} to participate in the valence cycling of iron.[30–32] Fig. 2f presents the high-resolution Fe 2p XPS spectra, which featured Fe(II) and Fe(III) components. Compared to Fe/Cu-700, the Fe(II) binding energy in Fe/Cu-800 shifts from 710.1 eV to 710.5 eV (+0.4 eV), yielding electron-deficient Fe(II), while the Fe(III) binding energy decreases from 712.5 eV to 712.2 eV (−0.3 eV). This "anisotropy" reflects

interfacial charge rearrangement and local electronic structure modulation at iron sites following copper introduction, enabling active Fe(II)/Fe(III) cycling. Fe(II) acts as an electron donor, cleaving the O–O bond of HSO_5^- to generate ROS (·OH) while being oxidized to Fe(III) in the PMS activation.[33,34] Copper serves as an electron shuttle, and interfacial coupling between the phases lowers electron-transfer resistance, thereby accelerating Fe(II) regeneration and enabling sustained highly efficient PMS activation.[33]

Electrochemical measurements such as electrochemical impedance spectroscopy (EIS), linear sweep voltammetry (LSV), and open-circuit voltage (OCV) were employed to further evaluate the charge transfer capability and stability of the catalysts. As shown in Fig. 2g, Fe/Cu-800 exhibited a significantly smaller arc radius than that of the other controls, indicating its lowest charge transfer resistance and most efficient interfacial charge transfer efficiency. Fig. 2h shows the semi-logarithmic polarization curves (E–log i) for Fe/Cu-700, Fe/Cu-800 and Fe/Cu-900, indicating typical cathodic/anodic branches and a minimum current point in the low-current region. The corresponding characteristic potentials were measured to be 1.047 V for Fe/Cu-700, 1.557 V for Fe/Cu-900, and 1.902 V for Fe/Cu-800, with the

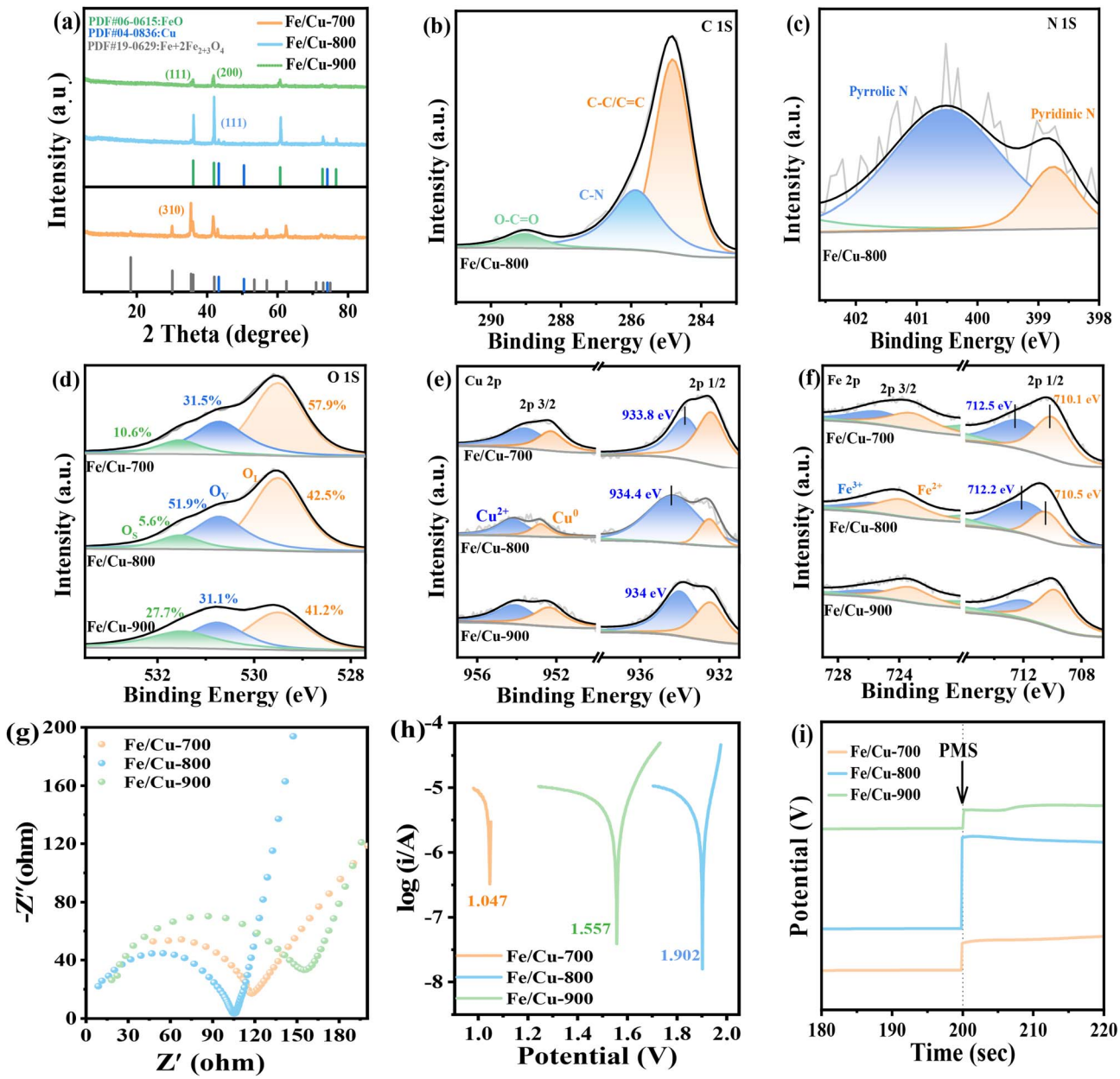

Fig. 2 (a) Wide-angle X-ray diffraction (XRD) patterns of Fe/Cu-700, Fe/Cu-800, and Fe/Cu-900. XPS core-level spectra of C 1s (b), N 1s (c), and O 1s (d) derived from Fe/Cu-800; Cu 2p (e) and Fe 2p (f) derived from Fe/Cu-700, Fe/Cu-800 and Fe/Cu-900. (g) Electrochemical impedance spectra (EIS) of the comparative catalysts, (h) linear sweep voltammetry (LSV) curves of the comparative catalysts, and the (i) open-circuit voltage (OCV) test curves of the comparative catalysts.

latter indicating a more favorable overall redox potential. Meanwhile, Fe/Cu-800 also exhibited the lowest current density at the cathodic trough, reflecting suppressed interfacial charge leakage and enhanced electrochemical stability. This combination promotes efficient electron transfer and sustains redox cycling during catalysis. OCP measurements (Fig. 2i) were employed to probe the electron transfer behavior among the catalysts and PMS. Upon the introduction of PMS, the OCP of all catalysts shifted markedly, confirming electron donation from the catalyst to PMS. Fe/Cu-800 exhibited the most pronounced potential shift, indicating its superior capability for PMS activation.[35]

3.3. Catalytic performance analysis

The catalytic performance of Fe/Cu-800 and other controls including Fe_3O_4-800, Fe/Cu-700, and Fe/Cu-900 was evaluated by monitoring the degradation of tetracycline (TC, 20 mg L^{-1}) in the presence of PMS. Fig. 3 presents the corresponding degradation kinetics results, the effects of reaction conditions, cycling stability, and the results of radical quenching experiments. As shown in Fig. 3a and S5, Fe/Cu-800 demonstrated the highest TC degradation rate under identical conditions, with activity following Fe/Cu-800 > Fe/Cu-900 > Fe/Cu-700. The presence of electron-deficient Fe(II) and Cu(II) sites further enhances PMS activation for ROS generation, while their coupled Fe^{2+}/Fe^{3+} and Cu^{+}/Cu^{2+} redox cycles sustain high catalytic activity.[31,36] The reaction kinetic constant further substantiated the superior performance of Fe/Cu-800, which exhibited the highest rate constant (0.235 min^{-1}). Its activity significantly surpassed that of Fe_3O_4-800 calcined under the same conditions, which is attributed to the introduced Cu species, which not only provide additional active sites through electron-deficient Cu(II) but also promote the dynamic transition of Fe valence states, thereby accelerating PMS activation.[37]

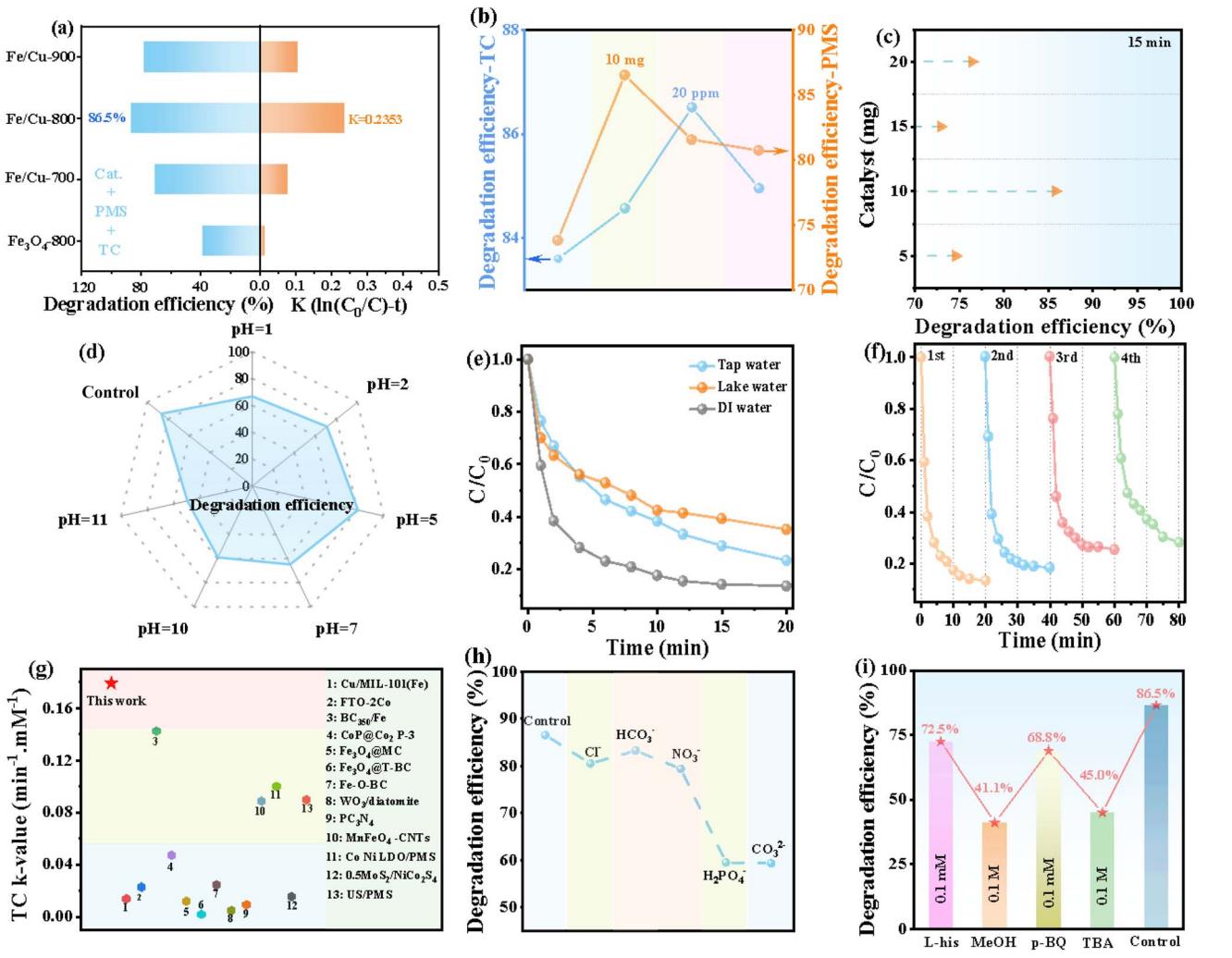

Fig. 3 (a) TC degradation performance of Fe_3O_4-800, Fe/Cu-700, Fe/Cu-800, and Fe/Cu-900, along with corresponding kinetic K values: relationship between $\ln(C_0/C)$ and reaction time; (b) the degradation efficiency of Fe/Cu-800 on TC at different TC concentrations and PMS doses, (c) different catalyst doses, (d) different pH conditions, and (e) different actual water sources; (f) TC degradation cycles of the Fe/Cu-800 catalyst, (g) TC degradation performance comparison with other reports; (h) effect of anionic interference, and (i) effect of quenching experiments.

To further determine the optimal reaction conditions for Fe/Cu-800, the effects of initial TC concentration, PMS dosage, and catalyst dosage on degradation performance were systematically investigated. Fig. 3b illustrates the TC degradation performance at varied TC concentrations and PMS dosages (Fig. S6). As the initial TC concentration increased, the degradation rate initially rose but then declined at higher loads, suggesting insufficient ROS availability at elevated pollutant levels.[38] Similarly, increasing the PMS dosage first enhanced the removal rate, but further addition led to reduced efficiency, likely due to radical self-quenching and competitive consumption.[39] As shown in Fig. 3c, the degradation rate increased with higher catalyst loading before plateauing and slightly decreasing at excessive amounts, which may be attributed to rapid PMS depletion and ineffective radical quenching on the catalyst surface, lowering the utilization efficiency of active species (Fig. S7).

Fig. 3d–f show the evaluation of the performance of Fe/Cu-800 across varying pH levels, in complex water matrices, and in cycling tests. The catalyst demonstrated stable activity over a wide pH range (Fig. S8), retained high degradation efficiency under complex water conditions, and showed minimal performance loss over four consecutive cycles. This confirmed its robust adaptability and stability, underscoring its potential for practical applications. Benchmark comparison with normalized PMS dosage (Fig. 3g) revealed that Fe/Cu-800 outperformed other reported catalysts in TC degradation (Table S1). The influence of common anions was also investigated (Fig. 3h and S9). The inhibitory effect on degradation followed the order: $CO_3^{2-} > H_2PO_4^- > NO_3^- > Cl^- > HCO_3^-$. The strong inhibition by CO_3^{2-} is likely related to solution alkalization, while $H_2PO_4^-$ may act *via* complexation or site passivation. In contrast, HCO_3^-, NO_3^-, and Cl^- showed relatively minor interference (Table S2).[40]

To investigate the metal composition of the catalysts at different calcination temperatures and their dissolution behavior during the reaction, ICP-OES analysis was performed. As shown in Tables S3 and S4, the Fe mass fraction increased progressively with calcination temperature, reaching 27.53%, 62.3%, and 77.63% for Fe/Cu-700, Fe/Cu-800, and Fe/Cu-900, respectively. In contrast, the Cu content remained nearly constant across all samples, ranging from 1.47% to 2.27%. This monotonic increase in Fe mass fraction does not indicate higher absolute Fe loading; rather, it reflects the relative enrichment of metallic components due to progressive graphitization and partial thermal decomposition of the polydopamine-derived carbon layer at elevated temperatures. This reduces the carbon content and correspondingly increases the relative Fe fraction. The consistent Cu content effectively rules out variations in Cu loading as a confounding factor in activity comparisons, confirming that the observed performance differences mainly arise from structural and phase-dependent characteristics. Regarding metal leaching, the concentrations of dissolved Fe and Cu in the reaction solutions remained low across all experimental groups. Fe leaching ranged from 0.289 to 0.790 ppm, while Cu leaching ranged from 0.049 to 1.638 ppm—both well below the limits specified by relevant water quality standards. The recovered catalysts retained 48% Fe and 1% Cu, indicating that the active metal sites remained largely intact under reaction conditions. The low levels of dissolved ions are insufficient to sustain an effective homogeneous catalytic cycle, suggesting that TC degradation is predominantly governed by heterogeneous catalytic processes rather than homogeneous Fenton-like reactions. Consequently, the risk of secondary metal contamination in practical wastewater treatment applications is minimal.[41]

To further identify the effects of various reactive active species on catalytic degradation reactions, radical quenching experiments were conducted (Fig. S10). Methanol (MeOH) is used for quenching $\cdot SO_4^-$ and $\cdot OH$, and tert-butanol (TBA) is used for quenching $\cdot OH$.[42] Since MeOH reacts with both radicals while TBA is selective for $\cdot OH$, their combined application allows the individual roles of $\cdot SO_4^-$ and $\cdot OH$ in the reaction to be differentiated. L-histidine (L-his) and *p*-benzoquinone (*p*-BQ) were employed to quench singlet oxygen ($^1O_2$) and superoxide anions (O_2^-), respectively.[43] As shown in Fig. 3i, the degradation rate of TC was significantly reduced after the addition of different radical quenchers, indicating that multiple active species were involved in the reaction process. Notably, the addition of MeOH and TBA resulted in the most pronounced inhibition, with a removal efficiency of 41.1% and 45%. It has been demonstrated that $\cdot OH$ plays a dominant role throughout the reaction process, while $\cdot SO_4^-$ contributes only about 4.9% to the overall reaction. In contrast, the addition of L-his and *p*-BQ exhibited relatively minor inhibitory effects, indicating that $^1O_2$ and $\cdot O_2^-$ contributed minimally to the reaction in this system. Quenching experiments indicate that multiple reactive species are involved, with $\cdot OH$ serving as the dominant oxidant in TC degradation. Collectively, these results demonstrate that the process is governed by a $\cdot OH$-dominated redox cycle driven by the electron-deficient Cu(II)/Fe(II) coupling pair:

$$Fe(II) + HSO_5^- \rightarrow Fe(III) + \dot{SO_4}^- + \cdot OH \quad (1)$$

$$Fe(III) + e^- \rightarrow Fe(II) \quad (2)$$

In this system, electron-deficient Cu(II) facilitates the reduction of Fe(III) by supplying electrons, thereby sustaining continuous regeneration of Fe(II) and enabling stable and efficient $\cdot OH$ production throughout the reaction. This electron-transfer-driven mechanism is fundamentally distinct from singlet oxygen pathways, which are neither thermodynamically nor structurally favored under the present reaction conditions.

3.4. Elucidation of the degradation pathway of TC

To elucidate the degradation pathways of tetracycline (TC), reaction intermediates were analyzed by liquid chromatography-mass spectrometry (LC-MS) (Text S2). The characteristic peak of TC (m/z = 444) disappeared after the reaction, and 20 major intermediates were identified.[44–50] These products indicate that double bonds, amino groups, and phenolic hydroxyl groups in TC are susceptible to attack by ROS ($\cdot OH$, $\cdot SO_4^-$ $\cdot O_2^-$, and $^1O_2$). Based on the identified intermediates, five primary degradation pathways are proposed (Fig. 4, Table S5). (I) Hydroxylation and oxidation at the C5 position

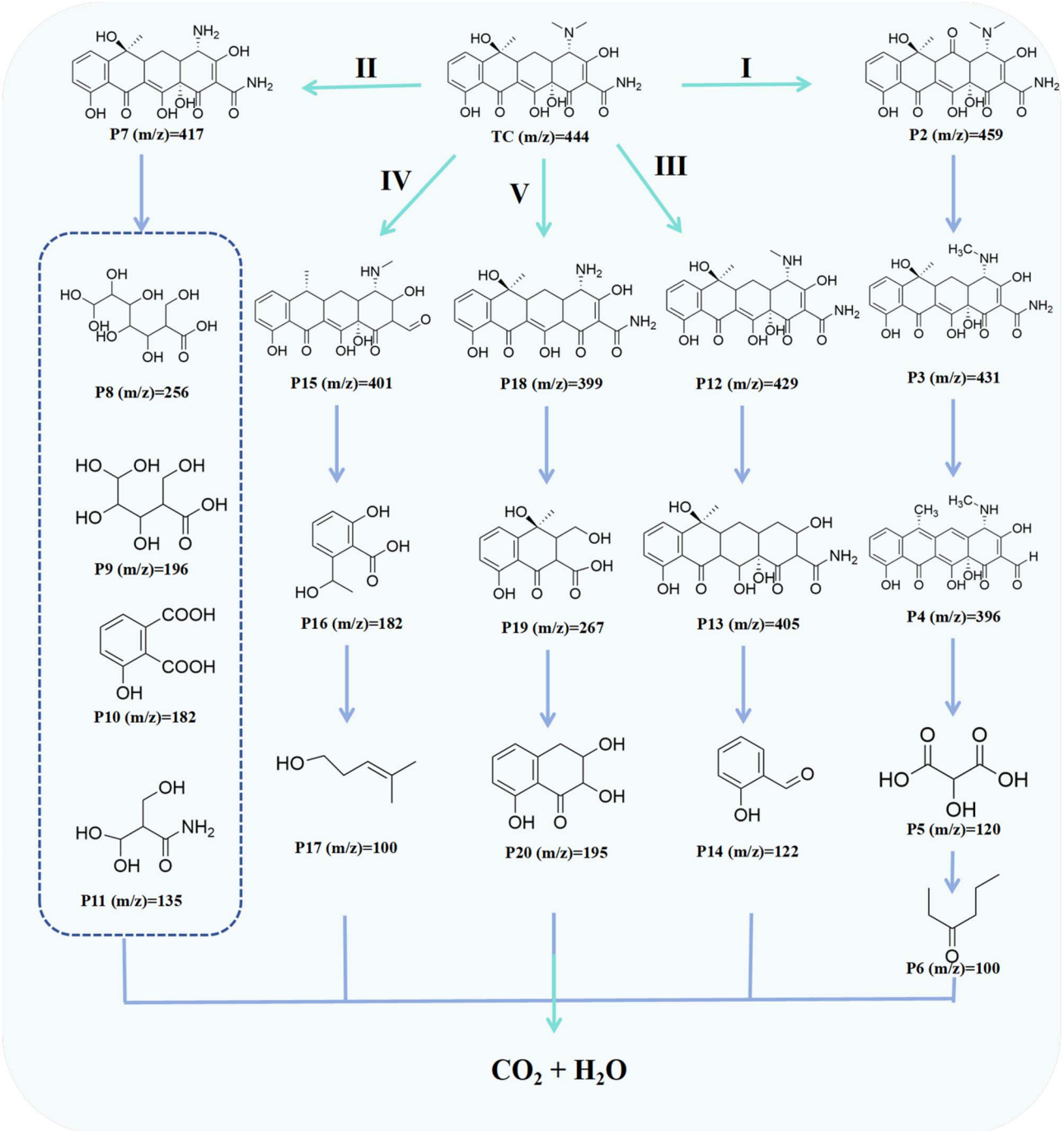

Fig. 4 Total mass spectra of TC degradation intermediates were obtained with the aid of LC-MS, and the TC degradation pathway was inferred from the AOP system.

form a ketone intermediate (P2), followed by *N*-demethylation (P3). Subsequent dealkylation, dehydration, and skeletal rearrangement yield P4, which undergoes ring-opening and decarboxylation to produce smaller molecules (P5 and P6). (II) Dealkylation and demethylation generate P7, which undergoes oxidative ring cleavage and backbone fragmentation to give intermediates P8–P11. These are further decarboxylated and oxidized. (III) Demethylation produces P12, and cleavage of the –$NHCH_3$ group yields P13. Further ring-opening and hydroxylation convert these into lower-molecular-weight product P14. (IV) Deamination at the C4 position, followed by intramolecular rearrangement with the C5 carbonyl, forms P15. Oxidative ring-opening, decarboxylation, and C–C bond cleavage produce P16, which is further converted *via* ring-opening and decarboxylation to P17. (V) Demethylation of the amino group gives P18, which undergoes decarboxylation and ring-opening to form P19 and P20. These intermediates are progressively cleaved and mineralized to CO_2 and H_2O. Overall,

the pathways involve repeated hydroxylation, demethylation, dealkylation, ring-opening, and decarboxylation, ultimately leading to the complete mineralization of TC.

To further validate the degradation and mineralization processes revealed by LC-MS, three-dimensional fluorescence spectroscopy was employed for supplementary analysis of the reaction system (Fig. S11). During the initial reaction phase, distinct fulvic acid-like fluorescence characteristics appeared in the 350–500 nm range, indicating that TC was first converted into organic intermediates with humic characteristics. As the reaction time increased, this fluorescence signal gradually weakened and eventually disappeared, suggesting that these intermediates were further oxidatively decomposed into low-molecular-weight substances and underwent continuous mineralization. These results are consistent with the degradation pathways and mineralization trends inferred from LC-MS.[43]

3.5. Toxicity analysis and evaluation of TC degradation intermediates

To further evaluate the ecological implications of the identified intermediates, QSAR-based tools, such as ECOSAR and T.E.S.T., were used to predict acute and chronic toxicity, developmental toxicity, mutagenicity, and bioaccumulation potential of TC and its degradation products across multiple aquatic and mammalian models (Fig. 5a–n, Text S3). The predicted toxicity of the major intermediates was consistently lower than that of the parent TC molecule. Moreover, log BCF values below 1 for most products indicated minimal bioaccumulation risk, collectively suggesting that Fe/Cu-800 facilitates environmentally benign degradation of TC. It should be noted, however, that QSAR predictions have inherent limitations in the applicability domain and quantitative accuracy; experimental verification of toxicity remains essential to strengthen ecological risk assessment in future studies. As shown in Fig. 5a, the predicted acute and chronic toxicity of P5, P8, P9, P10, and P11 was significantly lower than that of TC for all three test organisms. This indicates that the degradation pathway (II) is relatively ecologically benign, with only a few intermediates predicted to exhibit higher toxicity than the parent compound. The developmental toxicity of TC and its intermediates was further analyzed using the T.E.S.T. tool. The circular diagram shows progressively decreasing toxicity of intermediates predicted along the five degradation pathways, consistent with the expected trend during pollutant biodegradation (Fig. 5b, Text S3). Using the T.E.S.T. platform, the bioaccumulation potential of TC and its intermediates was predicted by calculating the log bioaccumulation factor (log BCF). As shown in Fig. 5c, most log BCF values were below 1, particularly for P8, P9, and P19, indicating extremely low bioaccumulation potential and minimal risk of bioaccumulation in food chains. Fig. 5d further demonstrates the decreasing trend of mutagenicity risk factors throughout the degradation process. As depicted in Fig. 5e–j,

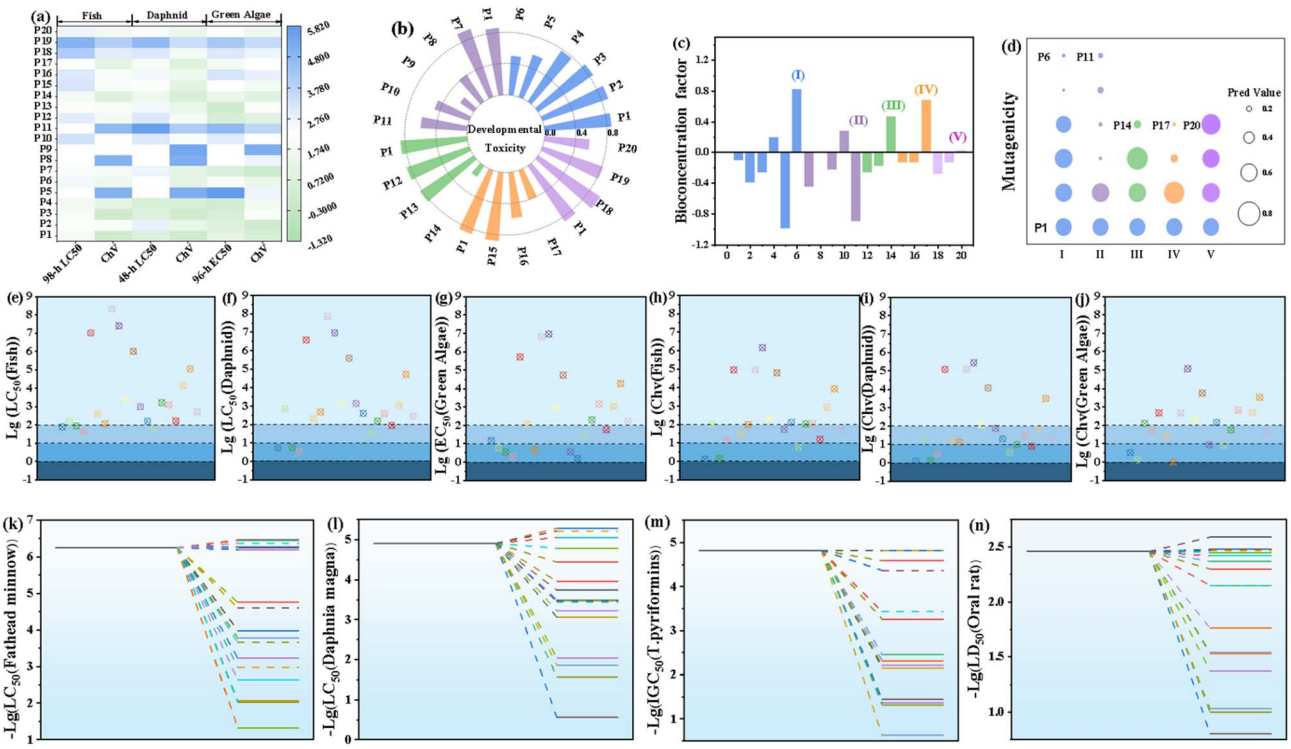

Fig. 5 (a) Analysis of the acute/chronic toxicity of TC and its degradation intermediates against fish, daphnid and green algae using the ECOSAR tool; (b) the developmental toxicity analysis; (c) bioconcentration factors; (d) assessment of the mutagenicity of the five degradation pathways of TC and its degradation intermediates using the T.E.S.T. tool; (e–j) the acute and chronic toxicity of TC and its resulting intermediates were analyzed using the ECOSAR program (Lg-value ≥ 2: no harmful; 1 ≤ Lg-value < 2: harmful; 0 ≤ Lg-value < 1: toxic; Lg-value ≤ 0: highly toxic); (k–n) the toxicity of TC and its resulting intermediates was analyzed using the T.E.S.T. program.

toxicity predictions for most intermediates fall within harmless or low-hazard levels, suggesting limited ecological risks based on these simulations. Finally, the T.E.S.T. tool was employed to simulate the combined toxicity of TC and its intermediates on the four model organisms: fathead minnow, Daphnia magna, Tetrahymena pyriformis and oral rat. As shown in Fig. 5k–n, nearly all intermediates exhibited lower toxicity than TC itself toward the first three organisms, and most intermediates also demonstrated reduced toxicity toward the rat oral model. Collectively, these findings demonstrated that the composite catalyst Fe/Cu-800 promotes the environmentally friendly degradation of TC.

3.6. Expanded dual-function application of the catalysts

Solar evaporation represents a sustainable and efficient approach for desalination and wastewater purification. In this study, we leverage the localized surface plasmon resonance (LSPR) effect of metallic copper and the broad-spectrum light absorption of black FeO to construct an efficient photothermal catalyst.[51] This combination is designed to enhance solar energy conversion for simultaneous water evaporation and pollutant degradation. A 300 W xenon lamp, calibrated to 1.0 sun (1 kW m^{-2}), served as the light source. The photothermal catalyst (Fe/Cu-800) was integrated into a floating evaporator by dispersing it in a sodium alginate solution, impregnating a glass fiber substrate, and crosslinking with Ca^{2+}.

Fig. 6 presents the photothermal performance under simulated sunlight. Infrared thermal imaging recorded the surface temperature every 10 minutes (Fig S12). In tetracycline (TC) solution, the Fe/Cu-800-coated evaporator reached 40.1 °C within 60 minutes, like that (39.5 °C) attained in deionized water (Fig. 6a and b). Control experiments confirmed that both light irradiation and the catalyst are essential for efficient heating, as the temperature only reached 30.1 °C with light alone (without the catalyst on the glass fiber) and remained at 20.1 °C in the dark (Fig. 6c and d). Furthermore, the Fe/Cu-800 modified evaporator achieved a high-water evaporation rate of 1.313 kg m^{-2} h^{-1} in TC solution under illumination (Fig. 6e and f). The outstanding solar-driven evaporation performance is

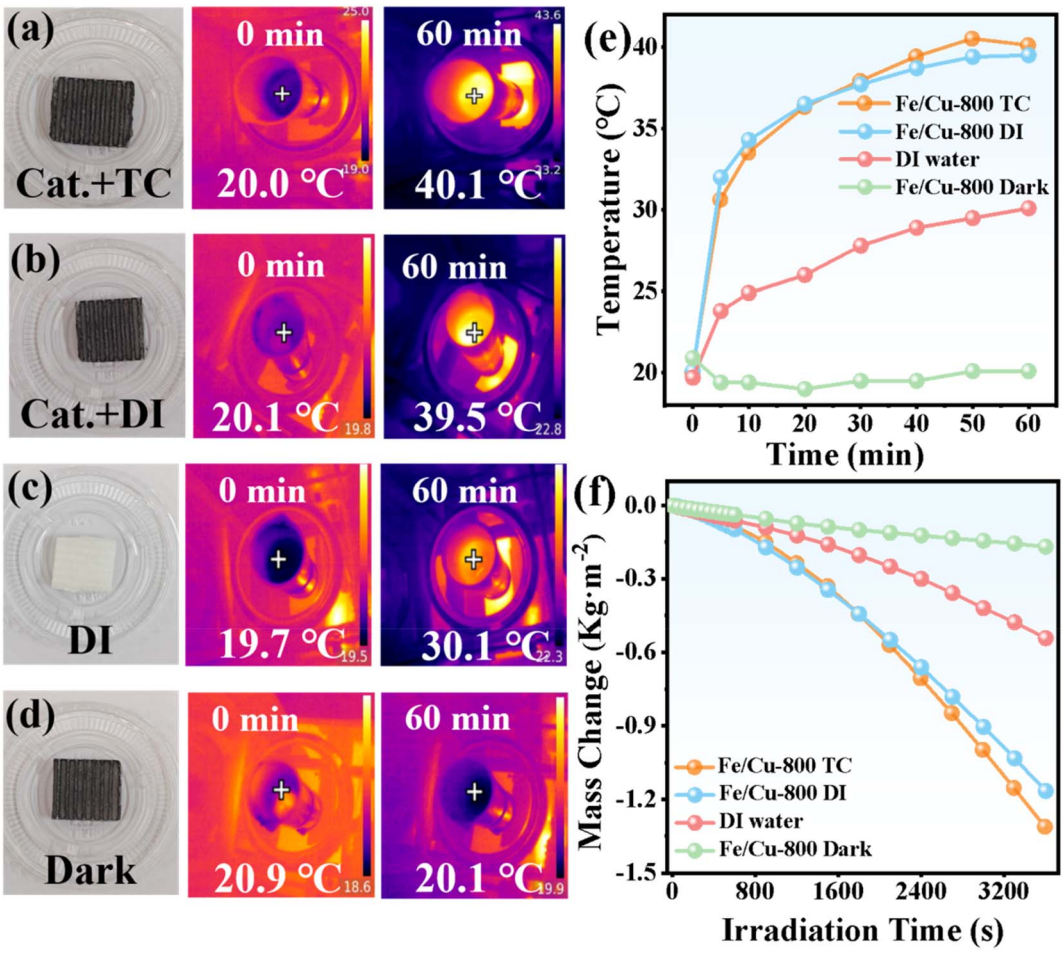

Fig. 6 (a) Infrared thermal images of Fe/Cu-800 modified glass fiber evaporating tetracycline solution under illumination; (b) infrared thermal images of Fe/Cu-800 modified glass fiber evaporating deionized water under illumination; (c) infrared thermal image of glass fiber evaporating deionized water under illumination; (d) infrared thermal image of Fe/Cu-800 glass fiber evaporating deionized water without illumination; (e) variation curve of membrane surface temperature over time during the water evaporation process as the irradiation time increases; (f) change in water quality over time during the photothermal evaporation process of the wet membrane.

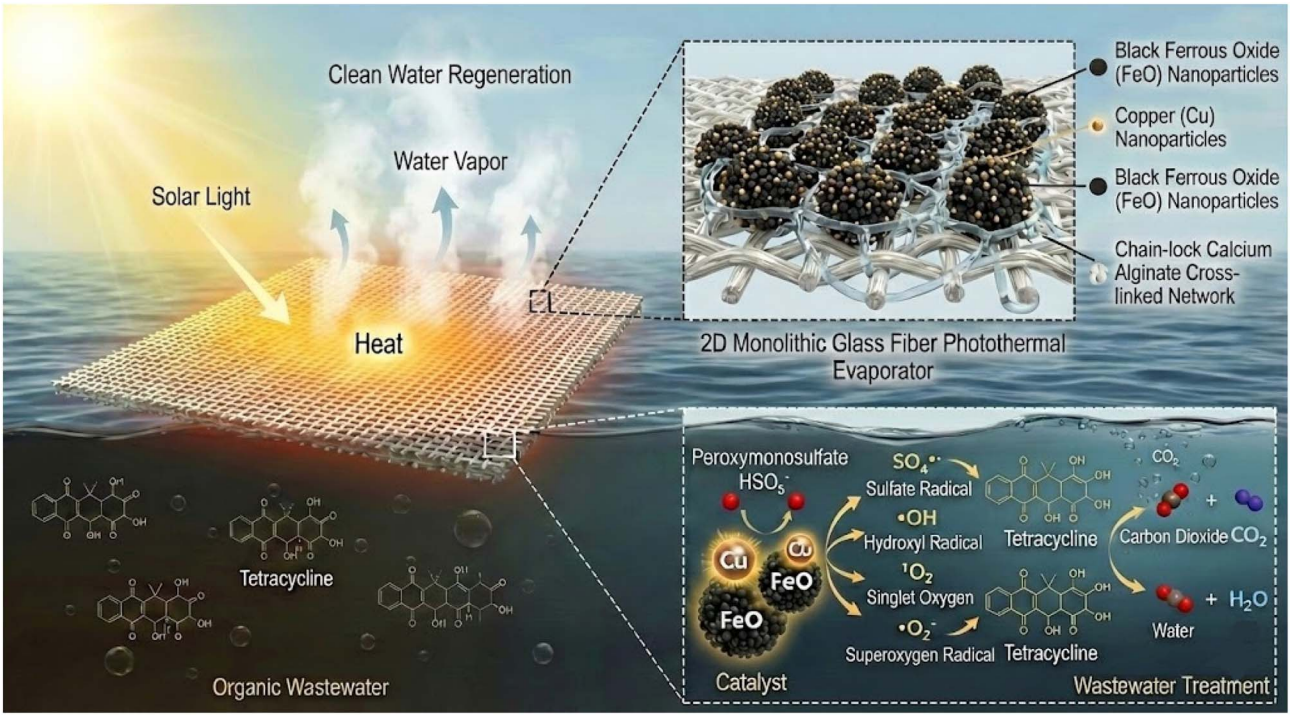

Scheme 1 Schematic diagram of TC degradation coupled with photothermal water evaporation in an integrated glass fiber Fe/Cu-800 evaporator.

attributed to the synergistic combination of plasmonic heating from Cu nanoparticles and broadband light absorption by FeO. To assess whether this photothermal effect enhances catalytic degradation, tetracycline (TC) removal experiments were conducted using the integrated evaporator under illumination (Fig. S12). The system achieved 94.4% TC removal within 20 minutes, with a rate constant of 0.1608 min^{-1}, substantially exceeding the sum of the rates observed in the catalyst-only and light-only control groups, demonstrating true photothermal synergy rather than simple additive effects (Fig. S13). Since solar-driven evaporation generates localized interfacial heating at the evaporator surface, complementary experiments were conducted at controlled temperatures of 20, 30, and 40 °C to quantify the effect of temperature on PMS activation kinetics (Fig. S14). The degradation rate increased with temperature, reaching optimal performance at 40 °C, consistent with the measured surface temperature under illumination. This confirms that localized heating effectively lowers the activation energy for Fe(II)-mediated PMS activation and accelerates the Fe^{2+}/Fe^{3+} redox cycling.[52–55] Taken together, these results demonstrate that the Fe/Cu-800 evaporator integrates efficient photothermal conversion with synergistically enhanced catalytic degradation, presenting a promising platform for solar-driven wastewater treatment.

Scheme 1 depicts a novel high-efficiency water treatment platform achieved through an integrated composite system crosslinked with the glass fiber and Fe/Cu-800 catalyst. This system simultaneously enables the oxidative degradation of TC and the regeneration of evaporated water. The Cu/FeO electronic defect pair in the Fe/Cu-800 catalyst enhances water vapor generation *via* photothermal conversion and promotes catalytic degradation reactions. During this process, the catalyst generates highly oxidative ·OH, $\cdot SO_4^-$, and $\cdot O_2^-$ radicals and the non-radical species $^1O_2$, effectively degrading the organic pollutant TC in water. This integrated reactor demonstrates outstanding performance in wastewater treatment, offering new insights into the application of multifunctional materials for environmental remediation, which is particularly significant for treating complex wastewater streams.

4. Conclusions

In summary, precise regulation of the calcination temperature enabled a directional phase transition from Fe_3O_4 to FeO, leading to the *in situ* formation of a Cu(II)/Fe(II) active pair with electronic defect characteristics at the Cu/FeO bimetallic interface. This fundamentally alters the electronic distribution at the interface, endowing the active sites with enhanced electron-accepting capabilities. Compared with Fe_3O_4-800 and other control catalysts, Fe/Cu-800 exhibits markedly improved PMS activation efficiency, achieving a TC degradation rate constant of 0.235 min^{-1}. TC is efficiently mineralized through multiple pathways, with ·OH identified as the dominant reactive species, while the ecotoxicity of degradation intermediates is significantly reduced.

Furthermore, by leveraging the localized surface plasmon resonance of Cu nanoparticles and the broadband light absorption of FeO, the catalyst was incorporated into a monolithic glass fiber evaporator to create a dual-function platform

integrating degradation and evaporation. Under 1-sun irradiation, the system achieved a water evaporation rate of 1.313 kg m^{-2} h^{-1}, enabling simultaneous pollutant degradation. The localized high temperature at the interface, induced by the photothermal effect, further accelerates PMS activation kinetics.

This work elucidates how temperature-driven phase transitions regulate the electronic structure of catalysts, providing a novel strategy for designing high-performance bimetallic catalytic systems and achieving integrated, efficient wastewater purification alongside freshwater regeneration.

Conflicts of interest

The authors declare that they have no known competing financial interests or personal relationships that could have appeared to influence the work reported in this paper.

Data availability

All data supporting the findings of this study are included in the supplementary information (SI). Supplementary information: Tables S1–S3, which summarize TC degradation performances in various catalyst/PMS systems, the effects of different inorganic anions on TC concentration over time, and detailed information on TC degradation intermediates; additional datasets are provided in Fig. S1–S11, including SEM images, FFT and XPS analyses, time-dependent catalytic degradation curves under various conditions, 3D fluorescence spectra, and infrared thermal images of the Fe/Cu-800 system. See DOI: https://doi.org/10.1039/d6ta00905k.

Acknowledgements

This work was financially supported by the National Natural Science Foundation of China (21908085), the Natural Science Foundation of Jiangsu Province, China (BK20241950), and the Ministry of Education, Singapore, under its Academic Research Fund Tier 1 (RG88/23).

References

1 Y. Lu, X. Zhou, Y. Zheng, H. Yang and W. Cao, *Water Res.*, 2025, **275**, 123179.
2 Y. Amangelsin, Y. Semenova, M. Dadar, M. Aljofan and G. Bjørklund, *Antibiotics*, 2023, **12**, 440.
3 Z. Mu, H. Zhao, W. Zhang, R. Ni, Z. Zhang, D. Shang, Y. Wang, Q. Wei, J. Pan and F. Yang, *Sep. Purif. Technol.*, 2026, **386**, 136535.
4 H. Zhu, Z. Wang, L. Cao, Y. Wang, Y. Zhang, D. Shang, L. Zhai, T. Yang and F. Yang, *Chem. Commun.*, 2025, **61**, 7065–7068.
5 O. E. Ohore, S. Zhang, S. Guo, B. Manirakiza, F. G. Addo and W. Zhang, *J. Hazard. Mater.*, 2021, **417**, 126148.
6 H. Zheng, Y. Ji, S. Li, W. Li and J. Ma, *Environ. Res.*, 2023, **227**, 115427.
7 Z. Zhou, Z. Shen, C. Song, M. Li, H. Li and S. Zhan, *Water Res.*, 2021, **201**, 117314.
8 Q. Zhou, C. Song, P. Wang, Z. Zhao and S. Zhan, *Proc. Natl. Acad. Sci. U. S. A.*, 2023, **120**, e2300085120.
9 E. Brillas, *J. Environ. Chem. Eng.*, 2024, **12**, 113191.
10 F. Miao, Z. Liu, X. Kang, C. Cheng, X. Mao, R. Li, H. Lin and H. Zhang, *Electrochim. Acta*, 2021, **377**, 138073.
11 S. Pan, X. Guo, X. Lu, R. Li, H. Hu, X. Nie, B. Liu, R. Chen, M. Zhu, S. Hei, X. Zhu, S. Zhang and H. Zhou, *Appl. Catal., B*, 2023, **330**, 122508.
12 K. Zhang, X. Min, T. Zhang, M. Si, W. Chen, Q. Wang, Y. Shi and L. Chai, *Chem. Eng. J.*, 2021, **423**, 129971.
13 S. Shao, X. Li, Z. Gong, B. Fan, J. Hu, J. Peng, K. Lu and S. Gao, *Chem. Eng. J.*, 2022, **438**, 135474.
14 N. Akram, W. Ma, J. Guo, Y. Guo, Z. Yansong, A. Hassan and J. Wang, *Chem. Phys.*, 2021, **540**, 110974.
15 Y. Liu, L. L. Liu, L. Y. Wang, M. L. Zang, L. Li and Y. K. Zhang, *Molecules*, 2024, **29**, 2217.
16 X. L. Zhao, Q. H. Zhang, J. F. Yang and X. Y. Wu, *J. Colloid Interface Sci.*, 2024, **673**, 669.
17 X. L. Zhao, X. Zhou, W. Y. Xing, Z. M. Yuan, K. L. Wang, Q. H. Zhang, Y. L. Shan, J. N. Liu, L. Ju, Z. Y. Jiang and H. He, *Mol. Catal.*, 2025, **570**, 114664.
18 H. Bai, P. He, L. Hao, Z. Fan, R. Niu, T. Tang and J. Gong, *Chem. Eng. J.*, 2023, **456**, 140994.
19 Y. Zheng, R. Ni, Y. Wang, Y. Zhang, L. Zhai, D. Shang, T. Yang, F. Yang and J. Pan, *Sep. Purif. Technol.*, 2025, **376**, 133988.
20 H. Zhao, E. Yuan, K. N. Opoku, M. Liu, X. Zhong, R. Ni, Z. Wang, Y. Wang, Z. Guo, C. Wang and F. Yang, *Chem. Eng. J.*, 2024, **500**, 156749.
21 Y. Xia, X. Li, Y. Qu, Y. Zhou, Z. Weng, S. Jin, J. Wang and X. Chang, *J. Mater. Chem. A*, 2025, **13**, 23035–23045.
22 Q. Wu and J. Li, *ChemElectroChem*, 2019, **6**, 1996.
23 O. N. Shebanova and P. Lazor, *J. Raman Spectrosc.*, 2003, **34**, 845–858.
24 X. Li, F. Liao, L. Ye and L. Yeh, *J. Hazard. Mater.*, 2020, **398**, 122938.
25 C. Lv and D.-L. Chen, *ChemCatChem*, 2024, **16**, e202401084.
26 J.-C. E. Yang, Y. Lin, H.-H. Peng, B. Yuan, D. D. Dionysiou, X.-D. Huang, D.-D. Zhang and M.-L. Fu, *Appl. Catal., B*, 2020, **268**, 118549.
27 J.-T. Lu, H.-W. Zhang, S. Li, S.-S. Guo, L. Shen, T.-T. Zhou, H. Zhong and L. Wu, *Inorg. Chem.*, 2020, **59**, 3152–3159.
28 T. Liu, S. Xiao, N. Li, J. Chen, X. Zhou, Y. Qian, C.-H. Huang and Y. Zhang, *Nat. Commun.*, 2023, **14**, 2881.
29 Y. Zhai, X. Ren, Y. Sun, D. Li, B. Wang and S. Liu, *Appl. Catal., B*, 2023, **323**, 122091.
30 Y. Liu, S. Hu, X. Zhang and S. Sun, *J. Colloid Interface Sci.*, 2023, **639**, 464–471.
31 P. Xu, P. Wang, X. Li, R. Wei, X. Wang, C. Yang, T. Shen, T. Zheng and G. Zhang, *Chem. Eng. J.*, 2022, **440**, 135863.
32 J. Liu, J. Liu, Z. Zhang, Y. Xu, N. Yang, Z. Wu, J. Lin, J. Shi and H. Deng, *J. Hazard. Mater.*, 2025, **492**, 138118.
33 C. Wang, W. Zhang, J. Wang, P. Xia, X. Duan, Q. He, I. Sirés and Z. Ye, *Appl. Catal., B*, 2024, **342**, 123457.

34 G. P. Anipsitakis and D. D. Dionysiou, *Environ. Sci. Technol.*, 2004, **38**, 3705–3712.
35 M. Y. Lan, Y. H. Li, C. C. Wang, H. Y. Zhu, D. H. Shang, L. Z. Zhai, Y. Y. Wang, T. Y. Yang and F. Yang, *Nat. Commun.*, 2024, **15**, 7208.
36 A. Xu, R. Chen, A. Khan, W. Zhao, J. Lin, R. Hu, W. Li, X. Liu, X. Li and S. Zhao, *Chem. Eng. J.*, 2024, **493**, 152489.
37 C. Yan, X. Cai, X. Zhou, Z. Luo, J. Deng, X. Tian, J. Shi, W. Li and Y. Luo, *J. Colloid Interface Sci.*, 2025, **678**, 858–871.
38 Y. Yang, W. Ji, X. Li, H. Lin, H. Chen, F. Bi, J. Xu and X. Zhang, *J. Hazard. Mater.*, 2022, **424**, 127640.
39 L. Huang, X. Zhang, J. Cai, H. Jiang, Y. Pan, L. Liu, Z. Song, T. Sheng and L. Li, *Langmuir*, 2025, **41**, 27569–27581.
40 J. Wang and S. Wang, *Chem. Eng. J.*, 2021, **411**, 128392.
41 Z. Yuan, H. Miao, Z. Jiang, X. Zhao, S. Shi and X. Zhu, *Mol. Catal.*, 2025, **577**, 114962.
42 X.-R. Pan, F.-Y. Kong and M.-Y. Xing, *Res. Chem. Intermed.*, 2022, **48**, 2837–2855.
43 S. Jiang, H. Zhao, Z. Ma, H. Zhu, D. Shang, L. Zhai, Y. Wang, Y. Song and F. Yang, *Nanoscale*, 2025, **17**, 7076–7090.
44 H. Sun, F. Guo, J. Pan, W. Huang, K. Wang and W. Shi, *Chem. Eng. J.*, 2021, **406**, 126844.
45 K. Zhang, S. Kang, R. Jia and C. Wang, *Environ. Res.*, 2025, **278**, 121664.
46 P. Duan, F. Kong, X. Fu, Z. Han, G. Sun, Z. Yu, S. Wang and Y. Cui, *Environ. Res.*, 2024, **245**, 117971.
47 B. Li, C. Lai, P. Xu, G. Zeng, D. Huang, L. Qin, H. Yi, M. Cheng, L. Wang, F. Huang, S. Liu and M. Zhang, *J. Clean. Prod.*, 2019, **225**, 898–912.
48 M. Abinaya, K. Govindan, M. Kalpana, K. Saravanakumar, S. L. Prabavathi, V. Muthuraj and A. Jang, *J. Hazard. Mater.*, 2020, **395**, 122648.
49 T. Ni, Z. Yang, H. Zhang, L. Zhou, W. Guo, D. Liu, K. Chang, C. Ge and Z. Yang, *Appl. Surf. Sci.*, 2022, **604**, 154537.
50 M. H. Firooz, A. Naderi, M. Moradi, *et al.*, *Sci. Rep.*, 2024, **14**, 4954.
51 H. Ghasemi, G. Ni, A. M. Marconnet, J. Loomis, S. Yerci, N. Miljkovic and G. Chen, *Nat. Commun.*, 2014, **5**, 4449.
52 Q. Li and M. Song, *J. Taiwan Inst. Chem. Eng.*, 2019, **97**, 458–465.
53 X. Wang, W. Zeng, H. Zhang, D. Li, H. Tian, X. Hu, Q. Wu, C. Xin, X. Cao and W. Liu, *RSC Adv.*, 2019, **9**, 27050–27059.
54 S. Cao, J. Fan, W. Sun, F. Li, K. Li, X. Tai and X. Peng, *Chem. Commun.*, 2019, **55**, 12956–12959.
55 Q. Wu, Q. P. Gao, L. M. Sun, H. M. Guo and X. P. Sun, *Chin. J. Catal.*, 2021, **42**, 482–489.